Discovery of potent SOS1 inhibitors that block RAS activation via disruption of the RAS–SOS1 interaction

Roman C. Hillig[a,1], Brice Sautier[a,2], Jens Schroeder[a], Dieter Moosmayer[a], André Hilpmann[a], Christian M. Stegmann[a], Nicolas D. Werbeck[a], Hans Briem[a], Ulf Boemer[a], Joerg Weiske[a], Volker Badock[a], Julia Mastouri[a], Kirstin Petersen[a], Gerhard Siemeister[a], Jan D. Kahmann[b], Dennis Wegener[b], Niels Böhnke[a], Knut Eis[a], Keith Graham[a], Lars Wortmann[a], Franz von Nussbaum[a], and Benjamin Bader[a,1]

[a]Research and Development, Pharmaceuticals, Bayer AG, 13353 Berlin, Germany; and [b]Drug Discovery Services, Evotec AG, 22419 Hamburg, Germany

Edited by Mariano Barbacid, Spanish National Cancer Research Centre, Madrid, Spain, and approved December 24, 2018 (received for review July 27, 2018)

Since the late 1980s, mutations in the *RAS* genes have been recognized as major oncogenes with a high occurrence rate in human cancers. Such mutations reduce the ability of the small GTPase RAS to hydrolyze GTP, keeping this molecular switch in a constitutively active GTP-bound form that drives, unchecked, oncogenic downstream signaling. One strategy to reduce the levels of active RAS is to target guanine nucleotide exchange factors, which allow RAS to cycle from the inactive GDP-bound state to the active GTP-bound form. Here, we describe the identification of potent and cell-active small-molecule inhibitors which efficiently disrupt the interaction between KRAS and its exchange factor SOS1, a mode of action confirmed by a series of biophysical techniques. The binding sites, mode of action, and selectivity were elucidated using crystal structures of $KRAS^{G12C}$–SOS1, SOS1, and SOS2. By preventing formation of the KRAS–SOS1 complex, these inhibitors block reloading of KRAS with GTP, leading to antiproliferative activity. The final compound 23 (BAY-293) selectively inhibits the KRAS–SOS1 interaction with an IC_{50} of 21 nM and is a valuable chemical probe for future investigations.

RAS | SOS | fragment screen | crystal structure | small-molecule inhibitor

First linked to human cancer in 1982 (1–3), members of the RAS family of GTPases (which comprises *KRAS*, *NRAS*, and *HRAS*) have since been recognized as major oncogenes, occurring in up to 20 to 30% of human cancers (4–6). RAS proteins act as molecular switches that cycle between an active, GTP-bound state and an inactive, GDP-bound state. Activated by guanine nucleotide exchange factors (GEFs), RAS in its GTP-bound state interacts with a number of effectors. Return to the inactive state is driven by GTPase-activating proteins (GAPs), which down-regulate active RAS by accelerating the weak intrinsic GTPase activity by up to 5 orders of magnitude. For oncogenic RAS mutants, however, the GAP activity is impaired or greatly reduced, resulting in permanent activation, which is the basis of oncogenic RAS signaling (7); for example, through the RAS-RAF-MEK-ERK and RAS-PI3K-PDK1-AKT pathways, both essential to cell survival and proliferation (8). Direct inhibition of RAS has proved extremely challenging due to the picomolar affinity of GTP for its binding site, the lack of other well-defined pockets, and the interaction of RAS with GEFs, GAPs, and effectors via extended and flat protein–protein interaction surfaces that are difficult to drug by small molecules. Additionally, attempts to inhibit RAS indirectly by targeting farnesyl transferases have not yet yielded approved drugs (9). Based on the failure of all direct and indirect approaches so far, RAS has been generally considered undruggable. Recent strategies to directly inhibit RAS have focused on (*i*) targeting Cys12 of the oncogenic mutant $KRAS^{G12C}$ with covalent inhibitors, (*ii*) RAS–effector interactions to disrupt downstream signaling, or (*iii*) inhibiting the RAS–GEF interactions to prevent reloading with GTP (10). While the first two strategies have seen recent encouraging successes (11–14), targeting the RAS–GEF interactions has not yet generated potent inhibitors. Furthermore, whether mutant RAS proteins require GEF activity for full activation remains to be fully explored and may differ depending on the specific mutation (15). The most-studied GEF for RAS is the protein Son of Sevenless (SOS) for which two human isoforms, SOS1 and SOS2, are known (16). Attempts to inhibit the RAS–SOS interaction via peptides mimicking an orthosteric SOS helix identified hydrocarbon-stapled peptides with nanomolar affinity, but only low cellular activity (17, 18). Fragment-based screening, rational design, and high-throughput screening approaches led to identification of small molecules addressing the KRAS–SOS1 interaction, resulting in compounds with moderate micromolar affinity (19–22). Surprisingly, rather than inhibition, some of these binders activated the SOS1-mediated nucleotide exchange, resulting in biphasic modulation of RAS signaling through negative feedback on SOS1 (23).

Here, we report the identification of small molecules that efficiently inhibit the activation of KRAS by SOS1. We focused on

Significance

Mutants of *RAS* are major oncogenes and occur in many human cancers, but efforts to develop drugs that directly inhibit the corresponding constitutively active RAS proteins have failed so far. We therefore focused on SOS1, the guanine nucleotide exchange factor (GEF) and activator of RAS. A combination of high-throughput and fragment screening resulted in the identification of nanomolar SOS1 inhibitors, which effectively down-regulate active RAS in tumor cells. In cells with wild-type KRAS, we observed complete inhibition of the RAS-RAF-MEK-ERK pathway. In a mutant KRAS cell line, SOS1 inhibition resulted in a reduction of phospho-ERK activity by 50%. Together, the data indicate that inhibition of GEFs may represent a viable approach for targeting RAS-driven tumors.

Author contributions: R.C.H., B.S., J.S., D.M., A.H., C.M.S., N.D.W., H.B., K.P., G.S., J.D.K., D.W., N.B., K.E., K.G., L.W., F.v.N., and B.B. designed research; R.C.H., B.S., A.H., H.B., J.M., J.D.K., and D.W. performed research; R.C.H., B.S., J.S., D.M., A.H., C.M.S., N.D.W., H.B., U.B., J.W., V.B., J.M., K.P., G.S., J.D.K., D.W., N.B., K.E., K.G., L.W., and B.B. analyzed data; and R.C.H., B.S., J.S., L.W., and B.B. wrote the paper.

Conflict of interest statement: R.C.H. B.S., J.S., D.M., A.H., C.M.S., N.D.W., H.B., U.B., J.W., V.B., J.M., K.P., G.S., N.B., K.E., K.G., L.W., F.v.N., and B.B. are or have been employees and stockholders of Bayer AG. J.D.K. and D.W. are employees of Evotec AG. R.C.H., B.S., J.S., D.M., H.B., K.P., N.B., K.E., L.W., F.v.N., and B.B. are coauthors of a patent application.

This article is a PNAS Direct Submission.

Data deposition: The atomic coordinates and structure factors have been deposited in the Protein Data Bank, www.wwpdb.org [PDB ID codes 5OVD, 5OVE, 5OVF, 5OVG, 5OVH, and 5OVI (SOS1 complexes); 6EIE (SOS2); and 6EPL, 6EPM, 6EPN, 6EPO, and 6EPP (KRAS–SOS1 complexes)].

[1]To whom correspondence may be addressed. Email: roman.hillig@bayer.com or benjamin.bader@bayer.com.

[2]Present address: Medicinal and Synthetic Chemistry, Evotec SAS, 31036 Toulouse Cedex, France.

This article contains supporting information online at www.pnas.org/lookup/suppl/doi:10.1073/pnas.1812963116/-/DCSupplemental.

Published online January 25, 2019.

the oncogenic G12C mutant of KRAS because of its clinical importance in lung cancer (24). Taking a dual approach supported by structure-guided design, we combined results from fragment-based and high-throughput screening. This included elucidation of crystal structures of the $KRAS^{G12C}$–SOS1 complex, of SOS1 in complex with inhibitors, and of apo SOS2. We present selective and potent compounds with double-digit nanomolar affinity to SOS1, submicromolar antiproliferative activity in tumor cell lines, and synergistic combination potential with the covalent $KRAS^{G12C}$ inhibitor ARS-853 (12, 13).

Results

In our efforts to identify inhibitors of mutant RAS for cancer treatment, we initiated two parallel approaches: (*i*) a fragment screen was performed to identify inhibitors via KRAS–SOS1 complex stabilization, in analogy to the inhibition of the small GTPase ARF by brefeldin A (25); and (*ii*) a high-throughput screen (HTS) was designed to search for inhibitors of the enzymatic SOS1 nucleotide exchange activity, via binding either to KRAS or to SOS1.

Fragment Screen for Stabilizers of the $KRAS^{G12C}$–SOS1 Interaction. To identify dead-end stabilizers of the $KRAS^{G12C}$–SOS1 interaction, a ligand-observed NMR fragment screen for binders of the complex of $KRAS^{G12C}$ and the catalytic domain of wild-type SOS1 ($SOS1^{cat}$) was performed (Fig. 1*A*). A library of 3,000 fragments was screened by saturation transfer difference (STD)-NMR in pools of eight, resulting in 310 single hits that were then counterscreened with $KRAS^{G12C}$ and $SOS1^{cat}$ alone. Of 97 fragments binding exclusively to the $KRAS^{G12C}$–$SOS1^{cat}$ complex, 42 were selected for crystallization based on their STD-NMR signals. Signals in the STD spectra indicated binding of fragment hit **F1** exclusively to the preformed $KRAS^{G12C}$–$SOS1^{cat}$ complex, and not to $SOS1^{cat}$ or $KRAS^{G12C}$ alone (Fig. 1*A*).

Crystals of the $KRAS^{G12C}$–$SOS1^{cat}$ complex were obtained using $KRAS^{G12C\_SB}$, a $KRAS^{G12C}$ construct containing the mutation C118S to increase stability (26), as well as a triple mutation (D126E-T127S-K128R) identified in a surface mutation screen (*SI Appendix*, *Supplementary Materials and Methods*). These mutations enabled $KRAS^{G12C\_SB}$–$SOS1^{cat}$ to crystallize in the same crystal form as reported for HRAS–SOS1 (27). Soaking of the 42 fragments into $KRAS^{G12C\_SB}$–$SOS1^{cat}$ crystals resulted in 13 cocrystal structures, of which four (fragments **F1** to **F4**) are presented (Fig. 1*B* and *SI Appendix*, Fig. S1 and Table S1). Surprisingly, all 13 fragment hits did not bind within the KRAS–SOS1 interface but into a mainly hydrophobic pocket on SOS1 located immediately adjacent to KRAS (Fig. 1*B*). The same pocket was recently reported for fragment hits targeting HRAS–SOS1 (19) and for SOS1 activators (21, 22). Remarkably, fragments **F1**, **F3**, and **F4** induced a conformational shift in the binding pocket by triggering a side-chain rotation of Phe890, thereby opening a new back pocket (*SI Appendix*, Fig. S1*D*). This Phe-out conformation was also observed by Winter et al. (19) for some fragment hits and by Burns et al. (21) for HTS-derived activators of the KRAS–SOS interaction. The other 10 fragment hits, represented by **F2** (*SI Appendix*, Fig. S1*C*), left Phe890 in its Phe-in conformation.

SOS1 features two distinct RAS binding sites: a catalytic site and an additional allosteric RAS binding site (28). Superimposition of the cdc25 domains of the fragment-bound KRAS–SOS1 crystal structures reported here with the HRAS–SOS1 complex that has an additional HRAS molecule bound to the allosteric site (PDB ID code 1NVU) revealed that RAS engagement at the allosteric site does not affect the fragment binding site.

All fragment hits were characterized for their stabilizing or disrupting effect on the $KRAS^{G12C}$–$SOS1^{cat}$ complex using a 2D protein-observed NMR assay (29), a surface plasmon resonance (SPR) assay, and a biochemical assay that quantifies the equilibrium binding interaction of $KRAS^{G12C}$ and $SOS1^{cat}$ (see detailed assay descriptions in *SI Appendix*, *Supplementary Materials and Methods*). Fragment **F1** stabilized the $KRAS^{G12C}$–$SOS1^{cat}$ complex in all three assays: In the 2D NMR assay, this was indicated by the reduction of signals for ^{15}N-labeled $KRAS^{G12C}$ upon addition of **F1** (*SI Appendix*, Fig. S2*A*). In the SPR assay, addition of **F1** increased the amount of $KRAS^{G12C}$ binding to immobilized $SOS1^{cat}$ (Fig. 1*C*). In the interaction assay, **F1** resulted in an increased homogeneous time-resolved fluorescence (HTRF) signal (Fig. 1*D*) similar to reference **R1** (*SI Appendix*, Table S2), a compound previously shown to bind and activate SOS1 (22). Only fragment **F3** behaved similarly to **F1**, whereas **F2** and all other fragments showed no effect in the $KRAS^{G12C}$–$SOS1^{cat}$ interaction assay, no stabilizing effect in the SPR assay, and no (or only weak) disruption effects in the NMR assay. Fragment **F1** was therefore chosen as the starting point for optimization (see also *SI Appendix*, *Supplementary Results* for further details on the fragment hit prioritization and fragment binding modes).

F1 interacts with SOS1 via a π–π interaction with Phe890 in its new Phe-out position and forms two hydrogen bonds to Tyr884 and Asp887 (Fig. 1*B*). The aminomethyl moiety additionally forms a cation–π interaction with the side chain of Tyr884. In an attempt to optimize **F1**, synthesis of a broad set of variants was undertaken; however, none of the variants yielded any significant improvement in potency.

HTS and Initial Optimization. To screen the Bayer library, consisting of over 3 million compounds, we developed a miniaturized enzymatic assay quantifying the SOS1-mediated loading of a fluorescently labeled GTP analog onto $KRAS^{G12C}$, which results in an increased HTRF signal ("On-assay" in Fig. 2*A*). Hits were retested using a secondary assay monitoring the SOS1-catalyzed HTRF signal decrease by the deloading of a fluorescently tagged GDP analog preloaded onto $KRAS^{G12C}$ ("Off-assay" in Fig. 2*A*). This secondary assay efficiently removed not only artificial hits that inhibit the primary assay by quenching but also GTP-competitive hits that are inactive in the Off-assay due to the requirement of excess GTP for nucleotide exchange. All hits were characterized for their selectivity for mutant $KRAS^{G12C}$ and against wild-type KRAS ($KRAS^{WT}$). The SOS1-dependence of inhibition was tested using an assay measuring intrinsic nucleotide exchange of $KRAS^{G12C}$ in the absence of SOS1. We further checked whether hits impact the interaction between $KRAS^{WT}$–GTP and the RAS binding domain (RBD) of its downstream effector CRAF kinase ($CRAF^{RBD}$). Finally, we used thermal shift assays (TSAs) to analyze the interaction of the small molecules with either $KRAS^{WT}$, $KRAS^{G12C}$, or $SOS1^{cat}$ as indicated by a shift of the protein melting point to higher temperature compared with the protein alone.

We focused on a quinazoline series, represented by initial-hit compound **1** (Fig. 2*A*). Biochemical characterization revealed that **1** inhibited SOS1-mediated loading of $KRAS^{G12C}$ with GTP much more efficiently than the direct KRAS inhibitor, reference **R2** (29) (Fig. 2*A* and *SI Appendix*, Table S2). In contrast to GDP, compound **1** was equipotent in the On-assay and Off-assay. It did not affect intrinsic $KRAS^{G12C}$ nucleotide exchange or the nucleotide exchange of another small GTPase, CDC42, by its GEF DBS (*SI Appendix*, Table S3). Compound **1** inhibited $KRAS^{WT}$ and $KRAS^{G12C}$ activation with promising submicromolar potency and did not affect the KRAS interaction with $CRAF^{RBD}$ (*SI Appendix*, Table S3). Together, these initial biochemical data suggested that compound **1** could be a non–GDP-competitive inhibitor of KRAS or a SOS1 inhibitor.

To elucidate the mechanism of action, we performed a set of biophysical assays. TSA, isothermal titration calorimetry (ITC), and native mass spectrometry (native MS) showed binding to $SOS1^{cat}$ (Fig. 2*B*) rather than a direct interaction with KRAS (*SI Appendix*, Fig. S2). Compound **1** stabilized $SOS1^{cat}$, but not

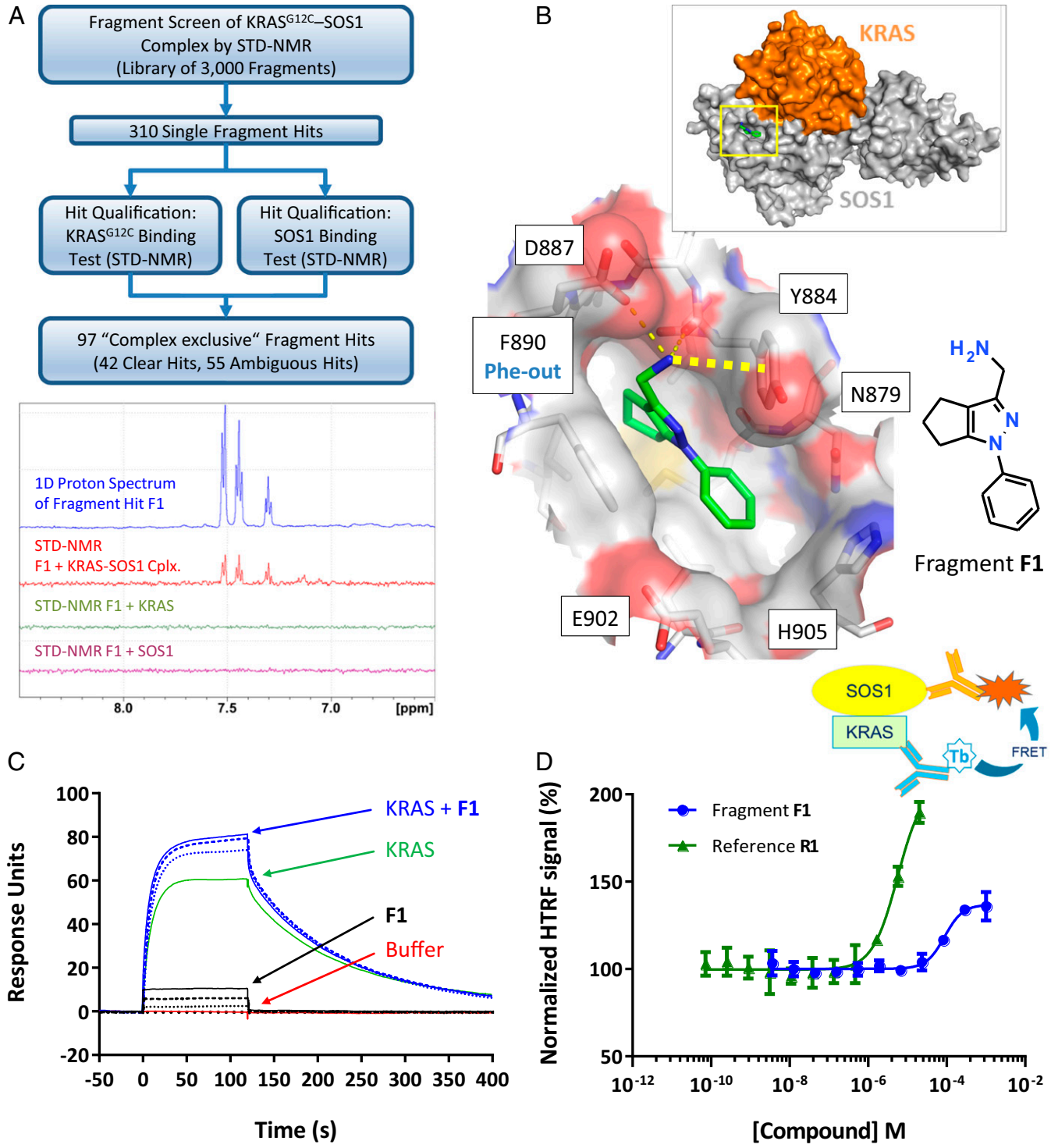

Fig. 1. $KRAS^{G12C}$–$SOS1^{cat}$ NMR fragment screen. (*A*) Screening cascade (*Top*) and example spectra for **F1** (*Bottom*): 1D proton spectrum (blue) and STD-NMR spectrum with $KRAS^{G12C}$–SOS1 complex (Cplx.; red), $KRAS^{G12C\_C118S}$ (green), and $SOS1^{cat}$ (purple). (*B*) Cocrystal structure of **F1** bound to $KRAS^{G12C}$–$SOS1^{cat}$. (*Top*) Overall complex with location of the fragment binding site (yellow box); *Inset* is the area in the yellow box enlarged, showing hydrogen bonds as thin dashed lines and cation–π interaction as a thick dashed line. (*C*) SPR assay with immobilized $SOS1^{cat}$. Green line: $KRAS^{G12C\_C118S}$; dotted, dashed, and solid blue lines: $KRAS^{G12C\_C118S}$ in the presence of 100, 250, and 500 μM **F1**, respectively; dotted, dashed, and solid black lines: respective addition of 100, 250, and 500 μM **F1** alone, showing unspecific binding of **F1** to $SOS1^{cat}$; and red line: buffer. (*D*) **F1** and the SOS-activator **R1** increase the interaction between $KRAS^{G12C\_C118S}$ and $SOS1^{cat}$. (*Top*) Assay scheme showing RAS, SOS1, and detection antibodies with fluorescent labels (Tb, terbium). (*Bottom*) Data points represent mean ± SD (n = 4). Normalization: 100% HTRF signal, DMSO control; 0% HTRF signal, without $SOS1^{cat}$.

$KRAS^{G12C}$ or $KRAS^{WT}$, in the TSA. ITC confirmed a strong enthalpy-driven binding of compound **1** to $SOS1^{cat}$, with a binding enthalpy, ΔH, of −14.1 kcal/mol, suggesting a favorable hydrogen bond network. The entropic penalty upon binding, $-T\Delta S$, contributes +5.5 kcal/mol, resulting in a K_D of 450 nM. Native MS confirmed binding of **1** to $SOS1^{cat}$, with a 1:1 stoichiometry, but not

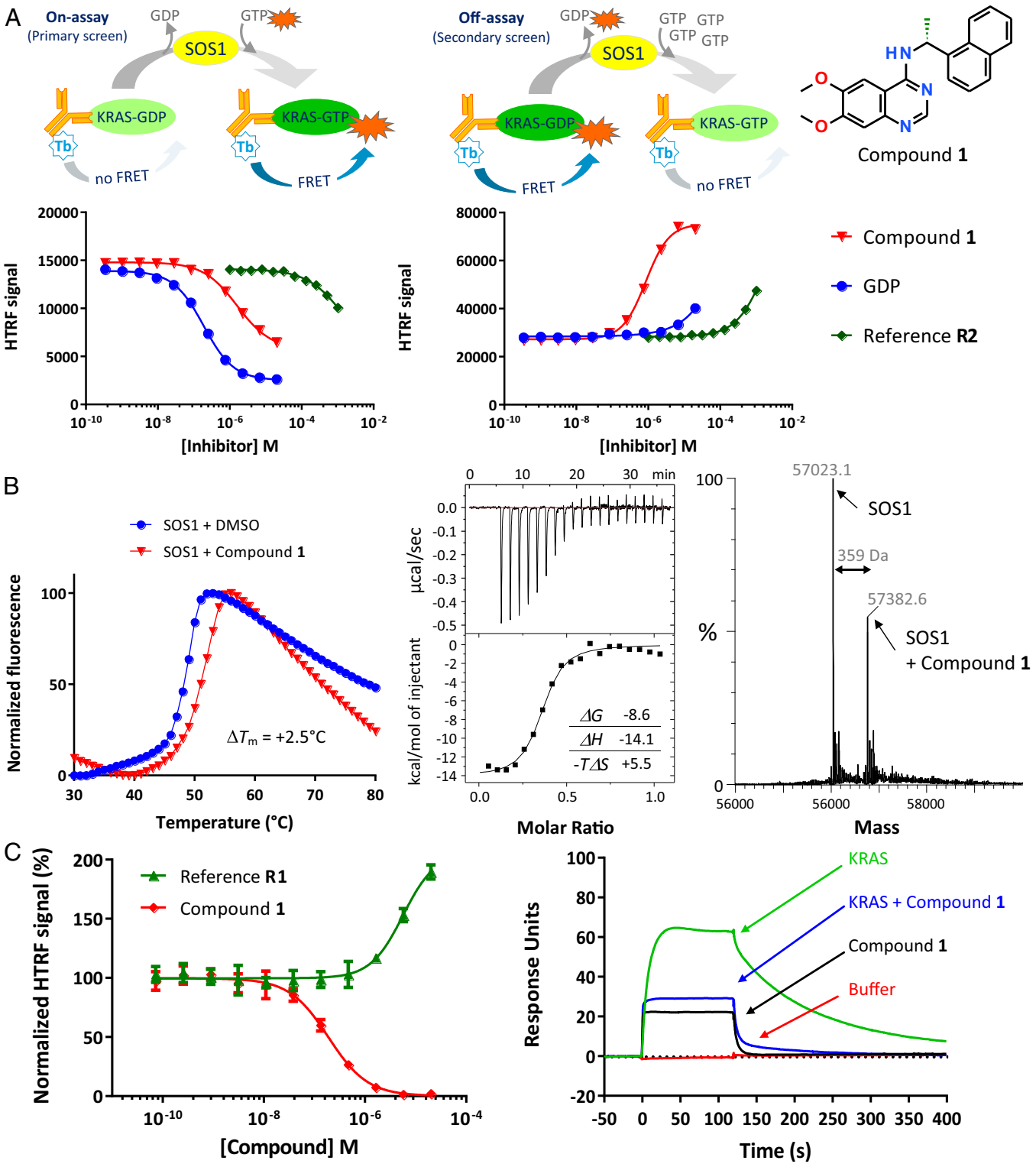

Fig. 2. Discovery of quinazolines as direct SOS1 inhibitors that disrupt the KRAS–SOS1 complex. (*A*, *Top*) Assay schemes (showing KRAS, fluorescently labeled GDP and GTP nucleotides, SOS1, and detection antibodies with fluorescent terbium label), and (*A*, *Bottom*) dose–response curves for GDP, compound **1**, and KRAS reference compound **R2** (*SI Appendix*, Table S2), shown for the On-assay (*Left*) and the secondary Off-assay (*Middle*). Data points represent mean ± SD ($n = 4$). (*B*, *Left*) TSA. Compound **1** stabilizes $SOS1^{cat}$ with a ΔT_m of 2.5 °C. (*B*, *Middle, Top*) ITC of the interaction of **1** with $SOS1^{cat}$. (*B*, *Middle, Bottom*) Heat curve of titration of $SOS1^{cat}$ into a solution of **1** and integrated enthalpies plotted against the protein-to-compound molar ratio. *Inset* shows thermodynamic values obtained from fitting a Wiseman isotherm to the measured calorimetric data. (*B*, *Right*) Native MS analysis confirmed binding of **1** to $SOS1^{cat}$ with a 1:1 stoichiometry. (*C*, *Left*) HTRF-based $KRAS^{G12C}$–$SOS1^{cat}$ interaction assay showing disruption of the $KRAS^{G12C}$–$SOS1^{cat}$ complex by **1** (red curve); the SOS activator **R1** (green curve, *SI Appendix*, Table S2) leads to a stabilization of the $KRAS^{G12C}$–$SOS1^{cat}$ complex. Data points represent mean ± SD ($n = 4$). Normalization as in Fig. 1*D*. (*C*, *Right*) SPR assay with immobilized $SOS1^{cat}$. Green: 250 nM $KRAS^{G12C\_C118S}$; blue: 250 nM $KRAS^{G12C\_C118S}$ in the presence of 10 µM compound **1**; black: 10 µM **1** alone, showing unspecific binding of **1** to $SOS1^{cat}$; and red: buffer. Compound **1** resulted in reduced binding of $KRAS^{G12C}$ to immobilized $SOS1^{cat}$.

to KRAS^{WT}. Additional experiments revealed the mode of action of this series as disruption of the KRAS^{G12C}–SOS1^{cat} interaction (Fig. 2*C*): Compound **1** addition led to a reduced FRET signal in the KRAS^{G12C}–SOS1^{cat} interaction assay in contrast to the SOS1 activator **R1**, which increased the FRET signal. Furthermore, addition of compound **1** resulted in a decreased amount of KRAS^{G12C} binding to immobilized SOS1^{cat}, as measured by SPR. Also, addition of compound **14** (a close derivative of **1**, see Fig. 3*D*) led to increased NMR signals for ^{15}N-labeled KRAS^{G12C_C118S}, indicative of disruption of the KRAS^{G12C}–SOS1^{cat} complex (*SI Appendix*, Fig. S2*B*).

To understand the molecular basis for the interaction with SOS1, we determined the cocrystal structure of SOS1 with compound **1** (Fig. 3*A* and *SI Appendix*, Table S4). Crystals were obtained with a variant of SOS1^{cat} with four additional N-terminal residues (termed SOS1^{SB}), first described by Freedman et al. (30).

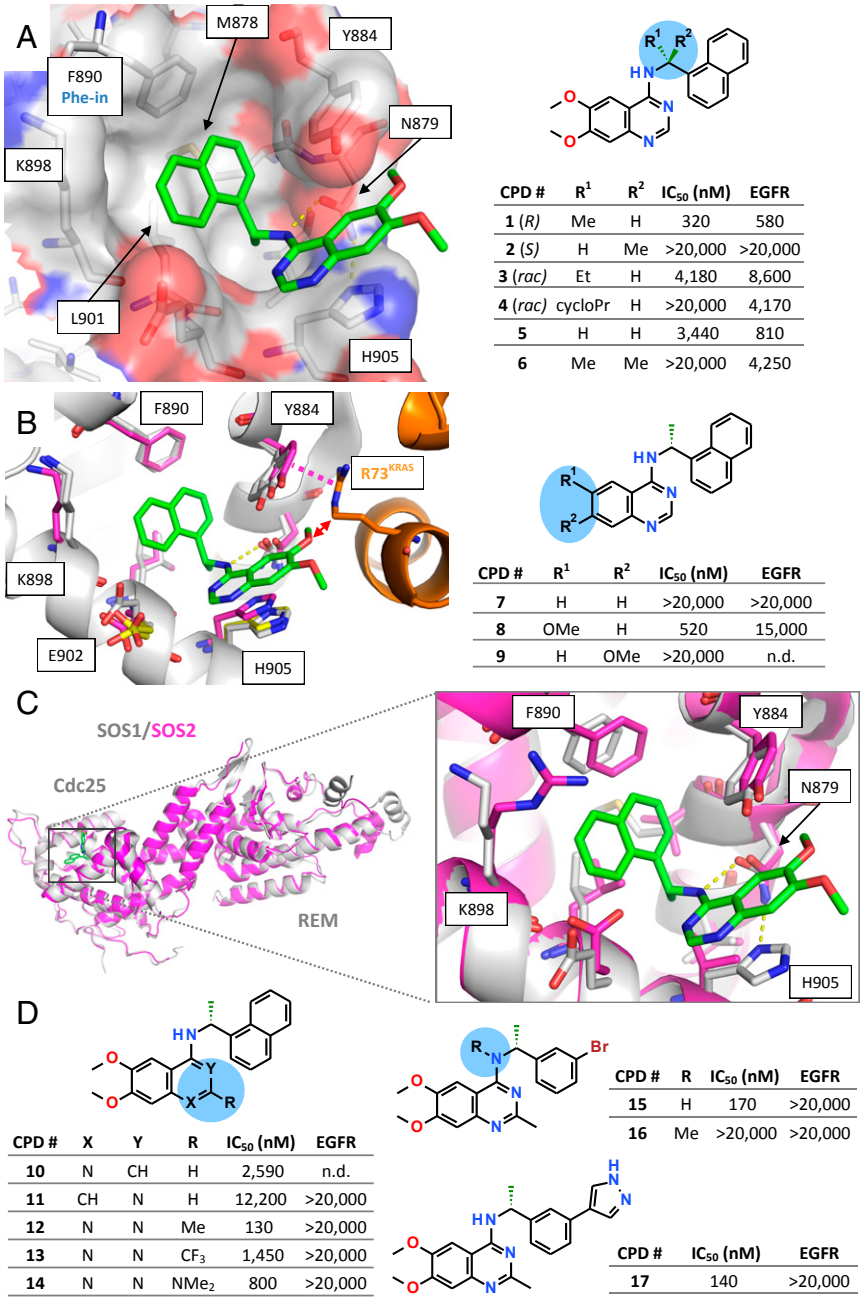

CPD #	R^1	R^2	IC_{50} (nM)	EGFR
1 (*R*)	Me	H	320	580
2 (*S*)	H	Me	>20,000	>20,000
3 (*rac*)	Et	H	4,180	8,600
4 (*rac*)	cycloPr	H	>20,000	4,170
5	H	H	3,440	810
6	Me	Me	>20,000	4,250

CPD #	R^1	R^2	IC_{50} (nM)	EGFR
7	H	H	>20,000	>20,000
8	OMe	H	520	15,000
9	H	OMe	>20,000	n.d.

CPD #	X	Y	R	IC_{50} (nM)	EGFR
10	N	CH	H	2,590	n.d.
11	CH	N	H	12,200	>20,000
12	N	N	Me	130	>20,000
13	N	N	CF_3	1,450	>20,000
14	N	N	NMe_2	800	>20,000

CPD #	R	IC_{50} (nM)	EGFR
15	H	170	>20,000
16	Me	>20,000	>20,000

CPD #	IC_{50} (nM)	EGFR
17	140	>20,000

Fig. 3. SOS1–compound **1** cocrystal structure, SAR, and crystal structure of SOS2. (*A*, *Left*) Cocrystal structure of SOS1^{SB} (carbon atoms in gray) in complex with **1** (stick model, carbon atoms in green). (*B*, *Left*) Crystal structure of SOS1^{SB} in complex with **1** (protein carbon atoms in gray, inhibitor carbon atoms in green), superimposed with the crystal structures of apo SOS1^{SB} (selected binding site residues shown, carbon atoms in yellow) and KRAS^{G12C_SB}–SOS1^{cat} (KRAS in orange, SOS1 carbon residues in magenta). Magenta dashed line indicates a stacking interaction between the side chain of Tyr884 and KRAS residue Arg73. Red arrow highlights a predicted clash between one of the two methoxy groups of the inhibitor with Arg73^{KRAS}. (*C*) Superimposition of the crystal structures of SOS1^{SB} (gray ribbon) in complex with **1** and apo SOS2^{SB} (magenta). Overall view (*Left*) and *Inset* view (*Right*) into the inhibitor binding site. (*A*, *Right and B*, *Right* and *D*) Initial SAR data for the SOS1 inhibitor series. IC_{50} values measured with the KRAS^{G12C}–SOS1^{cat} interaction assay and EGFR kinase inhibition assay (mean values; see *SI Appendix*, Table S8 for SD and biological replicates).

The inhibitor binds into a surface pocket on SOS1, which is located immediately adjacent to the KRAS binding site. The quinazoline scaffold is sandwiched between His905 and Tyr884 (π–π stacking). The naphthyl moiety occupies a hydrophobic pocket (formed by Leu901 and Phe890) and is in T-stacking contact with Tyr884. The central aniline NH function forms a hydrogen bond to the side chain of Asn879, an interaction shown to be essential, with complete loss of activity upon methylation of the free NH (see compound **16**, Fig. 3*D*). The key roles of Asn879, His905, and Leu901 were confirmed in a study in which mutations of these residues reduced the inhibitory effect of compound **1** (*SI Appendix*, Fig. S3). The methyl substituent at the stereocenter optimally occupies a small subpocket, which explains the observed eudysmic ratio, with the (*R*)-enantiomer **1** being active and the (*S*)-enantiomer **2** being inactive (Fig. 3*A*). The hydrophobic subpocket addressed by the naphthyl moiety is identical to the binding site reported above for the Phe-in binding fragment hits (*SI Appendix*, Fig. S1*C*). Comparison of the $SOS1^{SB}$–**1** complex with apo $SOS1^{SB}$ and with $KRAS^{G12C\_SB}$–$SOS1^{cat}$ indicated that the binding site for compound **1** is mostly already preformed in the absence of the ligand (Fig. 3*B*). The structures reveal how compound **1** weakens the KRAS–SOS1 interaction: Compared with the native $KRAS^{G12C}$–$SOS1^{cat}$ complex, compound **1** triggers a movement of the side chain of Tyr884 away from KRAS. This weakens the stacking interaction between this side chain and $Arg73^{KRAS}$. Remarkably, the two stabilizing fragments, **F1** and **F3**, also interact with the side chain of Tyr884 but, in doing so, stabilize this side chain in the conformation required for the interaction with $Arg73^{KRAS}$ (*SI Appendix*, Fig. S4). Also, the methoxy group at position 6 of compound **1** would clash with the side chain of $Arg73^{KRAS}$. This prediction from the structural data of the importance of the methoxy substitution at position 6 of the quinazoline core was experimentally confirmed by the synthesis and testing of compounds **7** to **9** (Fig. 3*B*). Thus, **7** and **9**, lacking substitution at position 6, are inactive, whereas **8**, with a single 6-methoxy group is as active as the initial hit **1**. The molecular basis for the observed disrupting mode of action of this inhibitor series therefore appears to be a combination of steric hindrance by the methoxy group and an indirect effect via the side chain of Tyr884.

SOS1, however, is only one of several exchange factors known to target the RAS family (16, 31). Its closest relative is SOS2 (80% identity in the catalytic domain), whereas the other known GEFs (e.g., RASGRF1/2 and RASGRP1 to RASGRP4) are less than 30% identical to SOS1. Despite the high sequence identity, selectivity assays with the quinazoline series revealed a strong selectivity against SOS2 (*SI Appendix*, Table S3). We were able to solve the crystal structure of the catalytic domain of SOS2 using a surface mutation approach (construct $SOS2^{SB}$). The overall fold is conserved between SOS1 and SOS2 (Fig. 3*C*). Comparison of the inhibitor-bound $SOS1^{SB}$ and apo $SOS2^{SB}$ crystal structures indicated that the observed selectivity can most likely be attributed to the exchange of $His905^{SOS1}$ to a valine residue in SOS2, which prevents the essential stacking interaction with the quinazoline core of compound **1** (Fig. 3*C*). Considering the much larger sequence differences between SOS1 and the other known RASGEFs, the quinazoline series of inhibitors is most likely also selective against the other exchange factors of RAS.

After identification of SOS1 as the molecular target and elucidation of the binding mode of the selected hit series, the structure–activity relationship (SAR) was explored. Consistent with the cocrystal structure of SOS1 with compound **1** (Fig. 3*A*), a methyl substituent at the benzylic position seems to be ideal. Thus, a sharp drop in potency was observed when methyl was replaced by a larger residue (compounds **3** and **4**) or, indeed, by hydrogen (compound **5**). Disubstitution at the benzylic position was not tolerated at all (compound **6**). The quinazoline motif proved to be essential for activity (Fig. 3*D*, **10** and **11**). Compound **1** shows structural similarity with known kinase inhibitors, such as the epidermal growth factor receptor (EGFR) kinase inhibitor erlotinib (32), and indeed inhibits EGFR kinase with an IC_{50} of 580 nM (*SI Appendix*, Table S3). To prevent interaction with the hinge region of kinases, an additional substituent was introduced at position 2, leading to the identification of 2-methyl-substituted quinazolines as compounds devoid of kinase inhibitory activity. Substituents in position 2 result in a steric clash with the hinge region of protein kinases and thereby abrogate the crucial interaction of the aminoquinazoline core with the hinge region, as illustrated for the case of the EGFR kinase inhibitor erlotinib (33) (*SI Appendix*, Fig. S5). The "dehinged" compound **12** indeed still strongly inhibited $SOS1^{cat}$ but also exhibited good selectivity against EGFR kinase (Fig. 3*D*), and the related compound **17** was inactive against a large panel of other kinases (*SI Appendix*, Table S5), including all kinases of the RAS-RAF-MEK-ERK pathway.

Guided by the cocrystal structure of SOS1 with compound **1**, we further optimized the quinazoline inhibitor series, culminating in compound **17**. Replacement of the naphthyl moiety by a pyrazolylphenyl group resulted in good potency and improved aqueous solubility, and the cocrystal structure (*SI Appendix*, Fig. S6*A*) revealed an additional water-bridged hydrogen bond to Glu902. However, the IC_{50} values of this series could not be optimized to better than 130 nM.

Linking of the HTS Hit Series with the Fragment Hit. As the fragment screen had identified a new subpocket that was not yet addressed by the HTS series, we aimed at further improving the potency by combining both ligand series. A superimposition of the cocrystal structures of compound **17** and fragment **F1** (Fig. 4*A*) suggested that hybrid compounds generated by linking the quinazoline inhibitor series to **F1** may show increased potency. Appropriate linkers that could orientate both the tetrahydrocyclopenta[*c*]pyrazole core of fragment **F1** and the aminoquinazoline core of compound **17** in their respective binding sites were designed by a computational approach using the software Spark (34). The overlapping aromatic groups were cut out, and appropriate replacements were identified in 3D databases of common building blocks and scored with respect to steric, geometric, and electrostatic properties (Fig. 4*A*). Most of the top-scoring linker candidates contained a five-membered aromatic heterocycle. For synthetic reasons, thiophene was selected as linker to investigate this hybrid approach.

Optimization of the hybrid series followed a two-pronged approach: initially, variants of the original fragment core of **F1** were fused to the thiophene linker; however, these hybrids failed to trigger the Phe-out conformation of Phe890 (see compound **18**, *SI Appendix*, Fig. S6*B*). In contrast, addition of moieties that mimic the hydrogen bonds of the amino side chain of **F1** resulted in improved IC_{50} values (Fig. 4*B*), and subsequent cocrystal structures revealed that both amino and hydroxyl groups trigger the Phe-out conformation: In the cocrystal structure with compound **21** (Fig. 4*B*), the hydroxyl group forms a new hydrogen bond to the backbone carbonyl of Tyr884. Cocrystallization with amino-containing racemate **22** revealed, unambiguously, that only the (*R*)-enantiomer **23** had bound in the crystal (Fig. 4*C* and *SI Appendix*, Table S4). The side-chain amino group of **23** forms two new hydrogen bonds, to Asp887 and Tyr884, and is in a favorable position for a cation–π interaction with the side chain of Tyr884 (see *SI Appendix*, *Supplementary Results* for a detailed analysis of the observed SAR of this hybrid series). Compound **23** was initially tested as a racemate (compound **22**), and later separated into the active (*R*)-enantiomer (**23**) and the weakly active (*S*)-enantiomer (**24**, eudysmic ratio ~111; Fig. 4*C*). Biophysical characterization of the active and less active enantiomers was performed. TSA confirmed binding of the racemate **22** and the active enantiomer **23** to $SOS1^{cat}$, while the less active

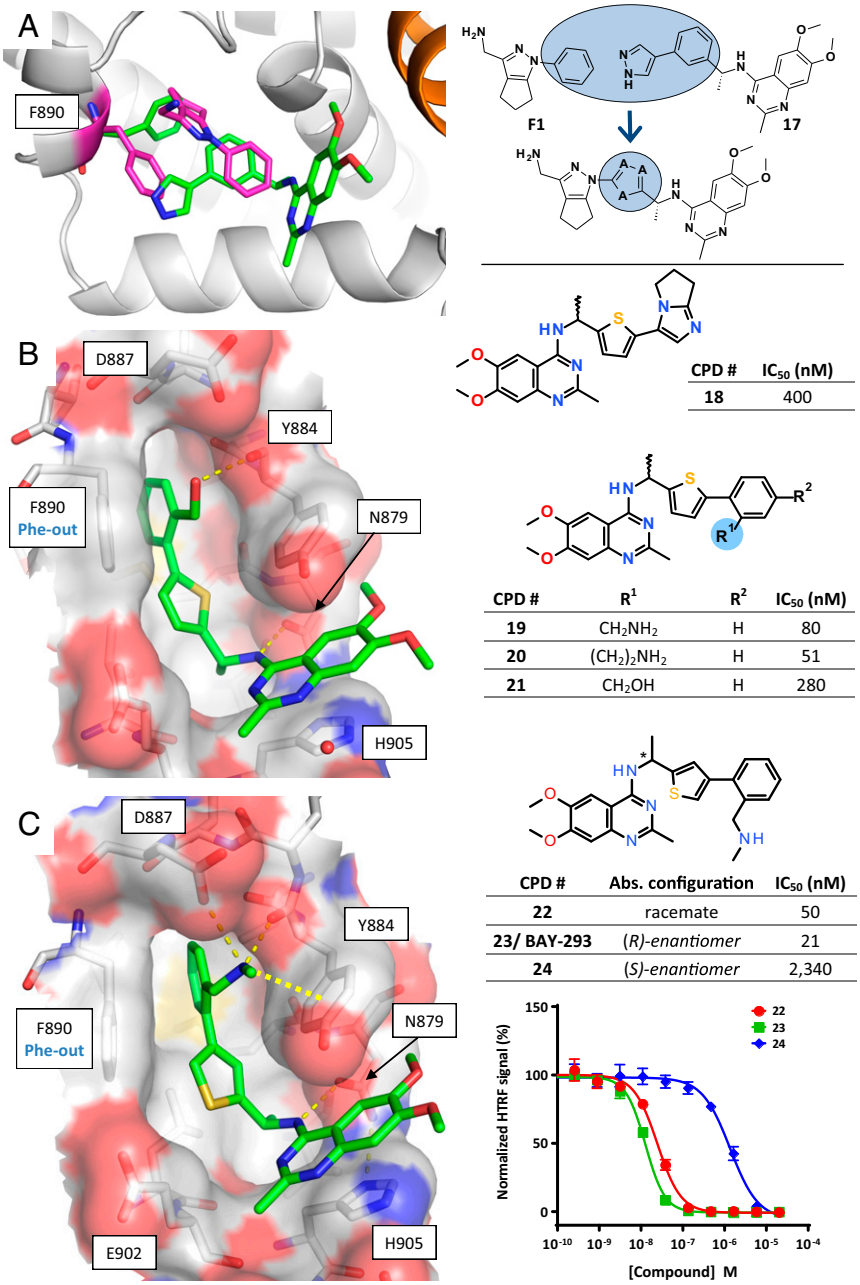

Fig. 4. Structure-based linking of the fragment and HTS hits. (*A*, *Left*) Superimposition of the crystal structures of **F1** bound to $KRAS^{G12C\_SB}$–$SOS1^{cat}$ (KRAS in orange, SOS1 in gray, **F1** and Phe890 with carbon atoms in magenta) and **17** bound to $SOS1^{SB}$ (only inhibitor and Phe890 shown; carbon atoms in green). (*Right*) Schematic depiction of the merging approach, with **18** as an initial example of the resulting hybrid compounds. (*B*, *Left* and *C*, *Left*) Crystal structures of $SOS1^{SB}$ in complex with **21** (*B*) and **23** (*C*); hydrogen bonds shown as thin dashed lines, cation–π interaction as a thick dashed line. (*B*, *Right* and *C*, *Right*) IC_{50} values measured with the $KRAS^{G12C}$–$SOS1^{cat}$ interaction assay (mean values; see *SI Appendix*, Table S8 for SD and biological replicates). (*C*, *Bottom Right*) Dose–response curves for compounds **22** to **24**.

variant **24** showed no stabilization of $SOS1^{cat}$. None of the three compounds stabilized $KRAS^{WT}$ or $KRAS^{G12C}$ (*SI Appendix*, Fig. S2*E*). The interaction of SOS1 with compounds **22**, **23**, and **24** was characterized by ITC. Binding was observed for racemate **22** and the active enantiomer **23**, but not for the less active enantiomer **24** (*SI Appendix*, Fig. S2*F*). The K_D values of 18 nM for **22** and 36 nM for **23** derived from the ITC binding curves were in line with the IC_{50} data obtained by the KRAS–SOS1 interaction assay (50 nM and 21 nM for **22** and **23**, respectively; Fig. 4*C*). Native MS analysis with $SOS1^{cat}$ showed a mass shift of 449 units with compound **23**, but not with compound **24** (*SI Appendix*, Fig. S2*G*). All optimized compounds of the HTS series showed a disrupting effect on the KRAS–SOS1 interaction, as shown for **22** and **23** in the interaction assay (Fig. 4*C*, *Right*). Compounds **22** and **23** were chosen as the best representatives of this inhibitor series before and after fusion with the fragment-derived moiety, respectively.

Cellular Characterization. The cellular activity of the quinazoline series was assessed by incubating HeLa cells with the SOS1 inhibitors, followed by quantification of the amount of activated, GTP-loaded total RAS from cellular lysates. Compounds

22 and **23** inhibited the activation of RAS in HeLa cells, with IC_{50} values in the submicromolar range, whereas the (*S*)-enantiomer **24** showed significantly lower activity (Fig. 5*A* and *SI Appendix*, Table S6).

Next, the downstream effects of the SOS1 inhibitors were analyzed by assays quantifying phospho-ERK (pERK) levels in K-562 cells, a tumor cell line for which sensitivity to SOS1 inhibition by CRISPR knockout has been reported (35). The racemate **22** and

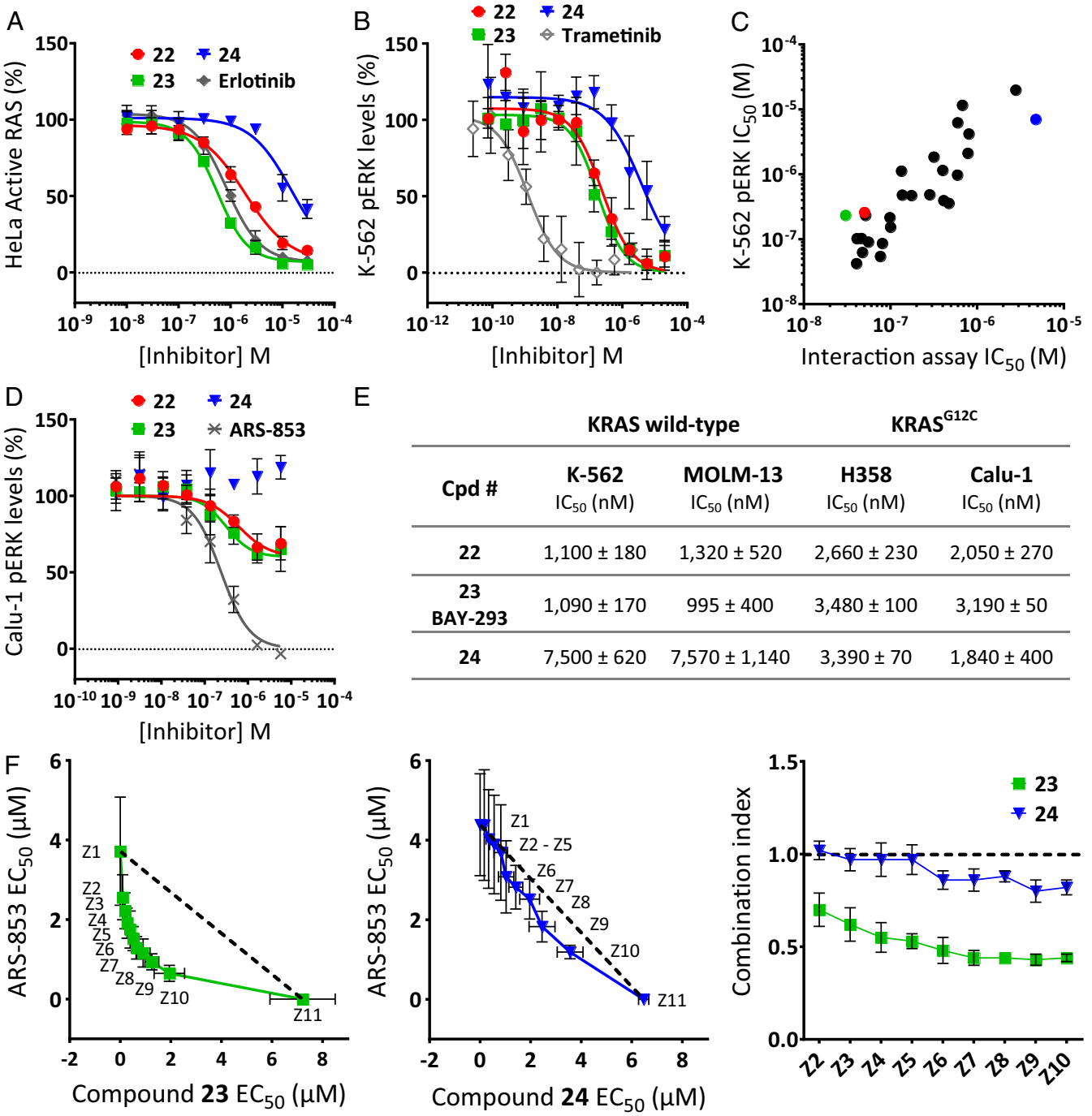

E

Cpd #	KRAS wild-type K-562 IC_{50} (nM)	KRAS wild-type MOLM-13 IC_{50} (nM)	$KRAS^{G12C}$ H358 IC_{50} (nM)	$KRAS^{G12C}$ Calu-1 IC_{50} (nM)
22	1,100 ± 180	1,320 ± 520	2,660 ± 230	2,050 ± 270
23 BAY-293	1,090 ± 170	995 ± 400	3,480 ± 100	3,190 ± 50
24	7,500 ± 620	7,570 ± 1,140	3,390 ± 70	1,840 ± 400

Fig. 5. Cellular characterization of compounds **22** to **24**. (*A*) Inhibition of active RAS levels in HeLa cells. (*B*) pERK levels in K-562 cells. (*C*) Correlation of IC_{50} data for pERK inhibition in K-562 cells with biochemical KRAS–SOS1 interaction. (*D*) pERK levels in Calu-1 cells. The colored dots represent compounds **22** (red), **23** (green), and **24** (blue). Reference compounds (*SI Appendix*, Table S2) in *A*, *B*, and *D* are indicated in gray. Data points in *A*, *B*, and *D* represent mean ± SD ($n = 4$). The IC_{50} values of **22** to **24** for these assays are summarized in *SI Appendix*, Table S6. (*E*) Antiproliferative activity against wild-type KRAS cell lines (K-562, MOLM-13) and cell lines with $KRAS^{G12C}$ mutation (NCI-H358, Calu-1). Mean IC_{50} values ± SD, $n = 4$. (*F*) Antiproliferative activity of **23** (*Left*) and **24** (*Middle*) was assessed in combination with the covalent $KRAS^{G12C}$ inhibitor ARS-853 in NCI-H358 cells. IC_{50} isobologram plots of SOS1-inhibitors (Z1) and ARS-853 (Z11) alone and of fixed combinations (Z2 to Z10) of both compounds are shown. The dotted line represents the line of additivity. Data points represent mean ± SD of biological independent experiments ($n = 3$). (*Right*) The combination index was calculated according to the median-effect model of Chou–Talalay (43); a value below 0.8 indicates a more-than-additive (i.e., a synergistic) interaction.

the (*R*)-enantiomer **23** efficiently inhibited pERK levels in K-562 cells after incubation for 60 min without affecting total protein levels of ERK, whereas the (*S*)-enantiomer **24** again showed significantly lower activity (Fig. 5*B* and *SI Appendix*, Fig. S8 for total ERK levels). Data from an extended set of compounds of our quinazoline inhibitor series revealed a significant correlation of the IC_{50} values measured by cellular pERK inhibition with biochemical inhibition of the KRAS–SOS1 interaction, indicating that the observed cellular effects of this inhibitor series are mediated by intracellular target engagement of SOS1 (Fig. 5*C*).

There is a common understanding that cells carrying mutant *KRAS* alleles are less dependent on their exchange factors than wild-type cells. To directly test this not-yet-fully explored hypothesis with our SOS1 inhibitors, we chose Calu-1 cells, which carry two $KRAS^{G12C}$ alleles. Analysis of total and pERK levels in these cells revealed that compounds **22** and **23** are able to inhibit pERK levels in a concentration-dependent manner. In contrast to the covalent $KRAS^{G12C}$ inhibitor ARS-853 (12, 13), the SOS1 inhibitors are not able to fully suppress downstream signaling, with ∼50% of the pERK levels remaining after treatment for 24 h (Fig. 5*D* and *SI Appendix*, Fig. S8 for total ERK levels).

Compound **22** was profiled for antiproliferative activity in 60 cell lines derived from lung, liver, and hematopoietic tissue (*SI Appendix*, Fig. S9). Compound **22** displayed a relatively broad inhibition spectrum, with hematopoietic cells (K-562, KG-1, MOLM-13, and THP-1) being most vulnerable to SOS1 inhibition. This is consistent with the previously identified SOS dependency of K-562 cells after SOS knockout by CRISPR (35). The antiproliferative activity of compounds **22** and **23** versus the less active enantiomer **24** was further studied in cells with wild-type KRAS (K-562, MOLM-13) and in cells with a $KRAS^{G12C}$ mutation (NCI-H358, Calu-1). In cells with wild-type KRAS, we found seven- to eightfold reduced activity of the less active enantiomer **24** compared with the racemate **22** and the pure active enantiomer **23** (Fig. 5*E*). In contrast, there was no significant difference between the active and less active compounds in cells carrying a $KRAS^{G12C}$ mutation.

Recent data suggest that SOS1 inhibition may have synergistic antiproliferative potential when combined with direct covalent $KRAS^{G12C}$ inhibitors. This is based on findings that (*i*) these covalent inhibitors selectively bind to the GDP-bound, but not to the GTP-bound, $KRAS^{G12C}$ protein and (*ii*) compared with other mutant KRAS proteins, $KRAS^{G12C}$ undergoes nucleotide cycling within cells and, therefore, requires reactivation by exchange factors (11, 13). With our potent SOS1 inhibitors, we were now able to test this hypothesis. We selected NCI-H358 cells, which are heterozygous for $KRAS^{G12C}$, and treated them with a combination of the covalent $KRAS^{G12C}$ inhibitor ARS-853 and either compound **23** or **24**. In contrast to the less active enantiomer **24**, synergy between **23** and ARS-853 was indeed observed (Fig. 5*F*, *Left*), with a combination index significantly below 0.8 over a wide range of combinations. These data suggest that parallel inhibition of SOS1 and $KRAS^{G12C}$ leads to synergistic antiproliferative activity and may therefore offer a viable option for the treatment of $KRAS^{G12C}$-mutant cancers in patients.

Discussion

This work describes a successful approach to identify nanomolar, selective, and cell-active inhibitors of SOS1, the exchange factor of RAS. The inhibitor design was enabled by a dual screening approach and structure-guided design. An HTS identified a core scaffold for which the potency was optimized to an IC_{50} of 130 nM (Figs. 2 and 3). A fragment screen identified an induced fit that opened a subpocket directly adjacent to the binding site of the HTS series (Fig. 1), also reported recently by Winter et al. (19) in a similar fragment-screening approach. Combination of both approaches was essential and led to the design of compounds addressing this subpocket, with an improved IC_{50} of 21 nM.

Remarkably, this binding site on the surface of SOS1, targeted by both the HTS hit series and the fragment hits, was reported initially as the binding site for activators of the SOS1-catalyzed nucleotide exchange of RAS (22). Consistent with this observation, two of the fragment hits acted as stabilizers and not disruptors of the $KRAS^{G12C}$–SOS1 interaction (Fig. 1). Fusing the binding functionality of one of these stabilizing fragments to the HTS-derived inhibitor series resulted in improved disruptors, not activators (Fig. 4). We suggest that the molecular basis for this functional flip is the stabilization of the side chain of Tyr884 in either a conformation optimal for π–π stacking with the KRAS residue Arg73, generating stabilizers (*SI Appendix*, Fig. S4), or in a conformation that is no longer able to engage in this stacking with $Arg73^{KRAS}$, generating disruptors (i.e., inhibitors, Fig. 3*B*).

Our nanomolar SOS1 inhibitors have allowed investigations of the effect of chemical SOS1 inhibition in cells. We could demonstrate that selective inhibition of SOS1 effectively downregulates the levels of active RAS in tumor cells. In cells with wild-type KRAS, we observed complete inhibition of the RAS-RAF-MEK-ERK pathway (Fig. 5*B*). In a tumor cell line with mutated *KRAS* alleles, chemical SOS1 inhibition resulted in a reduction of pERK activity by ∼50% (Fig. 5*D*). We investigated whether this still-limited downstream effect could be further improved by co-inhibition of additional targets. Indeed, covalent $KRAS^{G12C}$ inhibitors are known to require GDP-bound inactive $KRAS^{G12C}$ for binding, and potential combination therapies by upstream inhibition of RAS activation (e.g., by inhibition of receptor tyrosine kinase or RASGEF activity) have been discussed (11–13). We have shown that the combination of our SOS1 inhibitor with ARS-853, a covalent inhibitor of $KRAS^{G12C}$, results in synergistic antiproliferative activity in a $KRAS^{G12C}$-mutated cell line (Fig. 5*F*).

We therefore present compound **23** (BAY-293) as a tool for the further investigation of RAS–SOS1 biology in vitro. Improvements in the bioavailability of the inhibitor series will be required for in vivo experiments. Together, the data presented here indicate that inhibition of GEFs may represent a viable approach for targeting RAS-driven tumors. Of particular note is the synergistic effect between our inhibitors and ARS-853 observed in a $KRAS^{G12C}$-mutated cancer cell line, which highlights the potential for combination therapy between a direct KRAS and a SOS1 inhibitor.

Materials and Methods

DNA sequences for the recombinant proteins used in this study were optimized for expression in *Escherichia coli*, synthesized by GeneArt technology at Life Technologies, expressed in *E. coli*, and purified via affinity chromatography and size exclusion chromatography. All details of the cloning, expression, and purification steps are described in *SI Appendix, Supplementary Materials and Methods*. All expression constructs are listed in *SI Appendix*, Table S7. Quantification of $SOS1^{cat}$-mediated loading of human $KRAS^{G12C}$–GDP with a fluorescent GTP analog was carried out by measuring energy transfer from anti-GST-terbium (FRET donor) bound to GST-$KRAS^{G12C}$ after binding of a fluorescent GTP analog (FRET acceptor). Details of this assay and all secondary biochemical assays for $SOS1^{cat}$, $SOS2^{cat}$, $KRAS^{WT}$, $CRAF^{RBD}$, CDC42, and EGFR kinase are described in *SI Appendix, Supplementary Materials and Methods*.

Biophysical methods (TSAs, ITC, native MS, SPR complex assay, NMR methods) and crystallization methods are described in *SI Appendix, Supplementary Materials and Methods*. SOS1 inhibitors were cocrystallized with $SOS1^{SB}$. Fragments were soaked into pregrown crystals of $KRAS^{G12C\_SB}$–$SOS1^{cat}$. Datasets were collected at the Helmholtz-Zentrum Berlin in Germany, at the European Synchrotron Radiation Facility in Grenoble, France, or at the PETRA III synchrotron in Hamburg, Germany; processed using XDS (36) and XDSAPP (37); and solved using Molecular Replacement with Phaser (38) from the CCP4 suite (39). Models were rebuilt using Coot (40) and refined using REFMAC (41). Ligand models were generated using BIOVIA Discovery

Studio (Dassault Systèmes) and parameter files calculated with PRODRG (42). Figures were generated using PyMOL (Schrödinger, LLC).

The cell lines NCI-H358 and K-562 were obtained from the American Type Culture Collection. Calu-1 cells were obtained from CLS Cell Lines Service. MOLM-13 and HeLa cells were obtained from the German Collection of Microorganisms and Cell Cultures. Detailed information on the cellular assays is provided in *SI Appendix, Supplementary Materials and Methods*.

Fragments are commercially available from Enamine (**F1**, **F2**, and **F3**) and Asinex (**F4**). Detailed synthetic routes, procedures, and characterizations (compounds **1** to **45**, fragment **F1**) are available in *SI Appendix, Supplementary Materials and Methods*.

ACKNOWLEDGMENTS. We thank Dagmar Zeggert-Springer, Carmen Kropp, Marion Slezewski, Anne Sparmann, Jutta Hoffmann, Simone Thalheim, Linda Caparusagi, Katja Kauffeldt, Daniel Seifert, Patrick Zielinski, and Julian Plaga for technical support; the staffs at beamline BL14.1 at Helmholtz-Zentrum Berlin, at beamline P11 at PETRA III at the Deutsches Elektronen-Synchrotron (a member of the Helmholtz Association), and at beamline ID29 at the European Synchrotron Radiation Facility in Grenoble, for access to synchrotron radiation and support during data collection; the staffs at moloX GmbH for data collection services and at Crown Bioscience for performing the viability cell panel; and Hans Schick (Angewandte Synthesechemie Adlershof GmbH) and Qiuwen Wang (Pharmaron Beijing Co. Ltd.) and their teams for synthesis support.

1. Der CJ, Krontiris TG, Cooper GM (1982) Transforming genes of human bladder and lung carcinoma cell lines are homologous to the ras genes of Harvey and Kirsten sarcoma viruses. *Proc Natl Acad Sci USA* 79:3637–3640.
2. Parada LF, Tabin CJ, Shih C, Weinberg RA (1982) Human EJ bladder carcinoma oncogene is homologue of Harvey sarcoma virus ras gene. *Nature* 297:474–478.
3. Santos E, Tronick SR, Aaronson SA, Pulciani S, Barbacid M (1982) T24 human bladder carcinoma oncogene is an activated form of the normal human homologue of BALB- and Harvey-MSV transforming genes. *Nature* 298: 343–347.
4. Cox AD, Fesik SW, Kimmelman AC, Luo J, Der CJ (2014) Drugging the undruggable RAS: Mission possible? *Nat Rev Drug Discov* 13:828–851.
5. Hobbs GA, Der CJ, Rossman KL (2016) RAS isoforms and mutations in cancer at a glance. *J Cell Sci* 129:1287–1292.
6. Simanshu DK, Nissley DV, McCormick F (2017) RAS proteins and their regulators in human disease. *Cell* 170:17–33.
7. Haigis KM (2017) KRAS alleles: The devil is in the detail. *Trends Cancer* 3:686–697.
8. Downward J (2003) Targeting RAS signalling pathways in cancer therapy. *Nat Rev Cancer* 3:11–22.
9. Berndt N, Hamilton AD, Sebti SM (2011) Targeting protein prenylation for cancer therapy. *Nat Rev Cancer* 11:775–791.
10. Ostrem JM, Shokat KM (2016) Direct small-molecule inhibitors of KRAS: From structural insights to mechanism-based design. *Nat Rev Drug Discov* 15:771–785.
11. Janes MR, et al. (2018) Targeting KRAS mutant cancers with a covalent G12C-specific inhibitor. *Cell* 172:578–589.e17.
12. Lito P, Solomon M, Li LS, Hansen R, Rosen N (2016) Allele-specific inhibitors inactivate mutant KRAS G12C by a trapping mechanism. *Science* 351:604–608.
13. Patricelli MP, et al. (2016) Selective inhibition of oncogenic KRAS output with small molecules targeting the inactive state. *Cancer Discov* 6:316–329.
14. Sautier B, Nising CF, Wortmann L (2016) Latest advances towards ras inhibition: A medicinal chemistry perspective. *Angew Chem Int Ed Engl* 55:15982–15988.
15. Hunter JC, et al. (2015) Biochemical and structural analysis of common cancer-associated KRAS mutations. *Mol Cancer Res* 13:1325–1335.
16. Vigil D, Cherfils J, Rossman KL, Der CJ (2010) Ras superfamily GEFs and GAPs: Validated and tractable targets for cancer therapy? *Nat Rev Cancer* 10:842–857.
17. Patgiri A, Yadav KK, Arora PS, Bar-Sagi D (2011) An orthosteric inhibitor of the Ras-Sos interaction. *Nat Chem Biol* 7:585–587.
18. Leshchiner ES, et al. (2015) Direct inhibition of oncogenic KRAS by hydrocarbon-stapled SOS1 helices. *Proc Natl Acad Sci USA* 112:1761–1766.
19. Winter JJ, et al. (2015) Small molecule binding sites on the Ras:SOS complex can be exploited for inhibition of Ras activation. *J Med Chem* 58:2265–2274.
20. Evelyn CR, et al. (2014) Rational design of small molecule inhibitors targeting the Ras GEF, SOS1. *Chem Biol* 21:1618–1628.
21. Burns MC, et al. (2018) High-throughput screening identifies small molecules that bind to the RAS:SOS:RAS complex and perturb RAS signaling. *Anal Biochem* 548: 44–52.
22. Burns MC, et al. (2014) Approach for targeting Ras with small molecules that activate SOS-mediated nucleotide exchange. *Proc Natl Acad Sci USA* 111:3401–3406.
23. Howes JE, et al. (2018) Small molecule-mediated activation of RAS elicits biphasic modulation of phospho-ERK levels that are regulated through negative feedback on SOS1. *Mol Cancer Ther* 17:1051–1060.
24. Stephen AG, Esposito D, Bagni RK, McCormick F (2014) Dragging ras back in the ring. *Cancer Cell* 25:272–281.
25. Renault L, Guibert B, Cherfils J (2003) Structural snapshots of the mechanism and inhibition of a guanine nucleotide exchange factor. *Nature* 426:525–530.
26. Mott HR, Carpenter JW, Campbell SL (1997) Structural and functional analysis of a mutant Ras protein that is insensitive to nitric oxide activation. *Biochemistry* 36: 3640–3644.
27. Boriack-Sjodin PA, Margarit SM, Bar-Sagi D, Kuriyan J (1998) The structural basis of the activation of Ras by Sos. *Nature* 394:337–343.
28. Margarit SM, et al. (2003) Structural evidence for feedback activation by Ras.GTP of the Ras-specific nucleotide exchange factor SOS. *Cell* 112:685–695.
29. Sun Q, et al. (2012) Discovery of small molecules that bind to K-Ras and inhibit Sos-mediated activation. *Angew Chem Int Ed Engl* 51:6140–6143.
30. Freedman TS, et al. (2006) A Ras-induced conformational switch in the Ras activator Son of sevenless. *Proc Natl Acad Sci USA* 103:16692–16697.
31. Rojas JM, Oliva JL, Santos E (2011) Mammalian son of sevenless guanine nucleotide exchange factors: Old concepts and new perspectives. *Genes Cancer* 2:298–305.
32. Cruz-López O, et al. (2011) Novel substituted quinazolines for potent EGFR tyrosine kinase inhibitors. *Curr Med Chem* 18:943–963.
33. Stamos J, Sliwkowski MX, Eigenbrot C (2002) Structure of the epidermal growth factor receptor kinase domain alone and in complex with a 4-anilinoquinazoline inhibitor. *J Biol Chem* 277:46265–46272.
34. Slater M, Vinter A (2013) XED force field and spark. *Scaffold Hopping in Medicinal Chemistry*, ed Brown N (Wiley-VCH, Weinheim), Vol 58, pp 195–213.
35. Wang T, et al. (2015) Identification and characterization of essential genes in the human genome. *Science* 350:1096–1101.
36. Kabsch W (2010) XDS. *Acta Crystallogr D Biol Crystallogr* 66:125–132.
37. Sparta KM, Krug M, Heinemann U, Mueller U, Weiss MS (2016) XDSAPP2.0. *J Appl Crystallogr* 49:1085–1092.
38. McCoy AJ, et al. (2007) Phaser crystallographic software. *J Appl Cryst* 40:658–674.
39. Winn MD, et al. (2011) Overview of the CCP4 suite and current developments. *Acta Crystallogr D Biol Crystallogr* 67:235–242.
40. Emsley P, Lohkamp B, Scott WG, Cowtan K (2010) Features and development of Coot. *Acta Crystallogr D Biol Crystallogr* 66:486–501.
41. Murshudov GN, et al. (2011) REFMAC5 for the refinement of macromolecular crystal structures. *Acta Crystallogr D Biol Crystallogr* 67:355–367.
42. Schüttelkopf AW, van Aalten DM (2004) PRODRG: A tool for high-throughput crystallography of protein-ligand complexes. *Acta Crystallogr D Biol Crystallogr* 60: 1355–1363.
43. Chou TC (2010) Drug combination studies and their synergy quantification using the Chou-Talalay method. *Cancer Res* 70:440–446.